Image-domain wavefield tomography with extended common-image-point gathers

Tongning Yang and Paul Sava
Center for Wave Phenomena, Colorado School of Mines

ABSTRACT
Waveform inversion is a velocity-model-building technique based on full waveforms as the input and seismic wavefields as the information carrier. Conventional waveform inversion is implemented in the data-domain. However, similar techniques referred to as image-domain wavefield tomography can be formulated in the image domain and use seismic image as the input and seismic wavefields as the information carrier. The objective function for the image-domain approach is designed to optimize the coherency of reflections in extended common-image gathers. The function applies a penalty operator to the gathers, thus highlighting image inaccuracies arising from the velocity model error. Minimizing the objective function optimizes the model and improves the image quality. The gradient of the objective function is computed using the adjoint-state method in a way similar to that in the analogous data-domain implementation. We propose an image-domain velocity-model building method using extended common-image-point gathers constructed at discrete locations in the image. Such gathers have the advantage over conventional common-image gathers that they are robust for imaging reflectors with a wide range of dips. The common-image-point gathers can extract the velocity information from steep reflectors imaged with a two-way wave propagator, this information improving accuracy of the gradient computation and vertical resolution of velocity estimates. The gathers moreover are effective in reconstructing the velocity model in complex geologic environments and can be used as an economical replacement for conventional common-image gathers in wave-equation tomography. A test on the Marmousi model illustrates successful updating of the velocity model using common-image point gathers and resulting improved image quality.

Key words: wavefield tomography, wave-equation, extended images, adjoint state method

1 INTRODUCTION

Building an accurate and reliable velocity model remains one of the biggest challenges in current seismic imaging practice. In regions characterized by complex subsurface structure, prestack wave-equation depth migration (e.g., one-way wave-equation migration or reverse-time migration) is a powerful tool for accurately imaging the Earth's interior (Gray et al., 2001; Etgen et al., 2009). Because these migration methods are very sensitive to model errors, their widespread use significantly drives the need for high-quality velocity models because these migration methods are very sensitive to model errors (Symes, 2008; Woodward et al., 2008; Virieux and Operto, 2009).

Waveform inversion (WI) represents a family of techniques for velocity model building using seismic wavefields (Tarantola, 1984; Woodward, 1992; Pratt, 1999; Sirgue and Pratt, 2004; Plessix, 2006; Vigh and Starr, 2008a; Plessix, 2009; Symes, 2009). This type of methodology, although usually regarded as one of the costliest for velocity estimation, has been gaining momentum in recent years, mainly because of its accuracy as well as advances in computing technology. The core of WI is using a wave equation (typically constant-density acoustic) to simulate wavefields as the information carrier. Usually WI is implemented in the data domain by adjusting the velocity model such that simulated and recorded data match (Tarantola, 1984; Pratt, 1999). This match is based on the strong assumption that the wave equation used for simulation is consistent with the physics of the Earth. This, however,

is unlikely to be the case when the Earth is characterized by strong (poro)elasticity. In data domain approaches, significant effort is often directed toward removing the components of the recorded data that are inconsistent with the assumptions used.

Velocity-model-building methods using seismic wavefields can be implemented in the image domain rather than in the data domain. Instead of minimizing the data misfit, the techniques in this category update the velocity model by optimizing the image quality, which is the cross-correlation of wavefields extrapolated from the data and from the source wavelet. The image quality is optimized when the data are migrated with the correct velocity model, as stated by the semblance principle (Al-Yahya, 1989; Yilmaz, 2001). The common idea is to optimize the coherency of reflection events in common-image gathers (CIGs) via velocity-model-updating. Since images are obtained using full waveforms, and velocity estimation also employs seismic wavefields as the information carrier, these techniques can be considered as a particular type of WI, and we refer to them as image-domain wavefield tomography (WT). Unlike traditional image-domain ray-based tomography methods, image-domain WT uses band-limited wavefields in the optimization procedure. Thus, this technique is capable of handling complicated wave propagation phenomena such as multi-pathing in the subsurface. In addition, the band-limited character of the wave-equation engine more accurately approximates wave propagation in the subsurface and produces more reliable velocity updates than do ray-based methods.

Sava and Biondi (2004a,b) describe the concept of wave-equation migration velocity analysis, which is one variation of image-domain WT. The method linearizes the downward continuation operator and establishes a linear relationship between the model perturbation and image perturbation. The model is inverted by exploiting this linear relationship and minimizing the image perturbation. Sava et al. (2005) demonstrate application of the technique to velocity model building in complex regions, and Sava and Vlad (2008) discuss its detailed numerical implementation. This methodology, however, is limited by its reliance on the one-way wave propagation operator, which constrains its ability to produce model updates in complicated geology with steep reflectors.

Differential semblance optimization (DSO) is another variation of image-domain WT. The essence of the method is to minimize the difference of any given reflection between neighboring offsets or angles. Symes and Carazzone (1991) propose a criterion for measuring coherency within offset gathers and establish the theoretic foundation for DSO. The concept is then generalized to space-lag (subsurface-offset) and angle-domain gathers (Shen and Calandra, 2005; Shen and Symes, 2008). In practice, space-lag gathers (Rickett and Sava, 2002; Shen and Calandra, 2005) and angle-domain gathers (Sava and Fomel, 2003; Biondi and Symes, 2004) are two popular choices among various types of CIGs used for velocity analysis. These gathers are obtained by wave-equation migration and have fewer artifacts usually found in conventional offset gathers obtained by Kirchhoff migration, and thus they are suitable for applications in complex earth models (Stolk and Symes, 2004).

With recent developments in forward modeling and computing hardware, reverse-time migration (RTM) has become a common tool for imaging applications, especially in complex subsurface areas. One can characterize the wave propagation in the subsurface for the velocity estimation process more accurately using a two-way wave-equation propagator than using an one-way wave-equation propagator (Mulder, 2008). Furthermore, the capability of RTM for imaging steep reflections benefits velocity model building since more information can be extracted from the image to constrain the velocity updates (Gao and Symes, 2009). To effectively access the velocity information contained in steep reflections, Sava and Vasconcelos (2011) and Vasconcelos et al. (2010) propose common-image-point gathers (CIPs) as an alternative to space-lag or angle-domain gathers. CIPs are sparsely distributed in the subsurface on reflections and offer several advantages in the context of velocity inversion. First, the construction of a complete lag vector (space lags and time lag) avoids the bias toward nearly horizontal reflections. Thus, the gathers are sensitive to the velocity information in reflections with arbitrary dip and take advantage of the steep events imaged by RTM. Second, the discrete sampling of the gathers provides a flexible way to extract the velocity information from the image and facilitates target-oriented velocity updates. Furthermore, the sparse construction of the gathers reduces computational cost and storage requirements, both important in 3D applications.

In this paper, we propose an image-domain wavefield-based velocity-model-building approach using CIPs as the input. One key component of image-domain WT is wavefield simulation using a one-way or two-way wave-equation engine, similar to data-domain WI but with more flexibility. Another key component of the method is the objective function (OF), which is constructed by applying a penalty operator to CIPs whose minimization allows us to optimize image coherency and to update the velocity model simultaneously. The third component is an effective gradient calculation based on the adjoint state method (Plessix, 2006; Symes, 2009). In summary, gradient calculation with this method consists of the following steps: (1) compute the *state variables*, i.e., the seismic wavefields obtained from the source by forward modeling and from the data by backward modeling; (2) compute the *adjoint source*, i.e., a calculation based on the OF and on the state variables; (3) compute the *adjoint state variables*, i.e., the seismic wavefields obtained from the adjoint source by backward modeling; (4) compute the *gradient* using the state and adjoint state variables. We provide more details on this technique in the body of the paper.

This paper starts with a theoretical discussion of image-domain WT and its implementation with CIPs and CIGs. We show that CIPs overcome the bias toward nearly horizontal reflectors, which is important in the presence of steeply dipping structures because the information extracted from steep reflections provides additional constraints on the velocity model building. We use the Marmousi model to demonstrate that CIPs can be an economical and accurate replacement for CIGs

used in the conventional wave-equation-based DSO approach to model building in complex subsurface areas. The results obtained from CIPs are comparable to those obtained from CIGs, but with smaller cost for computing and storing the image gathers.

2 THEORY

In this section, we formulate image-domain wavefield tomography using both space- and time-lag extended images (extended CIPs) or space-lag extended images (also known as subsurface-offset CIGs). The gradient is computed by applying the adjoint-state method (Plessix, 2006; Symes, 2009), which is also a common practice for data-domain full-waveform inversion (Tarantola, 1984; Sirgue and Pratt, 2004; Virieux and Operto, 2009). This approach can easily be generalized to other image-domain wavefield tomography methods implemented with different input image gathers, e.g., time-lag CIGs (Yang and Sava, 2011).

For simplicity, we discuss the methodology in the frequency-domain rather than in the time-domain although the latter is completely equivalent and analogous. We formulate the inverse problem by first defining the state variables, through which the OF is related to the model parameters. The state variables for our problem are the source and receiver wavefields u_s and u_r obtained by solving the following acoustic wave equation:

$$\begin{bmatrix} \mathcal{L}\left(\mathbf{x},\omega,m\right) & 0 \\ 0 & \mathcal{L}^{*}\left(\mathbf{x},\omega,m\right) \end{bmatrix} \begin{bmatrix} u_s\left(j,\mathbf{x},\omega\right) \\ u_r\left(j,\mathbf{x},\omega\right) \end{bmatrix} = \begin{bmatrix} f_s\left(j,\mathbf{x},\omega\right) \\ f_r\left(j,\mathbf{x},\omega\right) \end{bmatrix} , \tag{1}$$

where f_s is the source function, f_r are the recorded data, $j = 1, ...N_s$, where N_s is the number of shots, ω is the angular frequency, and $\mathbf{x} = \{x, y, z\}$ are the space coordinates. The wave operator $\mathcal{L}$ and its adjoint $\mathcal{L}^*$ propagate the wavefields forward and backward in time, respectively, using either a one-way or two-way wave equation. In this formulation, we designate the operator $\mathcal{L}$ to be

$$\mathcal{L} = -\omega^2 m - \Delta \ , \tag{2}$$

where Δ is the Laplace operator, and model parameter m represents slowness squared.

In the second step of the adjoint-state method, we first construct the OF and then the adjoint sources that are used to model the adjoint-state variables required by the gradient computation. The OF for image-domain wavefield tomography is defined using the semblance principle (Yilmaz, 2001) and measures the image incoherency caused by the model errors. Therefore, the inversion process of minimizing the OF simultaneously reconstructs the model and improves the image quality.

We consider the objective function in the $\boldsymbol{\lambda} - \tau$ domain ($\boldsymbol{\lambda}$ is a vector that pertains to space-lags in 2D or 3D space and τ pertains to time-lag) and use extended CIPs as the input to analyze and optimize the velocity model. Extended CIPs are obtained by applying the nonzero space- and time-lag cross-correlation imaging condition (Sava and Fomel, 2006) to the wavefields at selected points in the image. Sava and Vasconcelos (2011) analyze the kinematic characteristics of reflections in extended CIPs and point out that reflections focus at zero space- and time-lags when the migration velocity is correct. Therefore, the OF based on extended CIPs is defined as

$$\mathcal{H}_{\boldsymbol{\lambda},\tau} = \frac{1}{2} \| K_I\left(\mathbf{x}\right) P\left(\boldsymbol{\lambda},\tau\right) r\left(\mathbf{x},\boldsymbol{\lambda},\tau\right) \|^2_{\mathbf{x},\boldsymbol{\lambda},\tau} \ , \tag{3}$$

where $P\left(\boldsymbol{\lambda},\tau\right)$ is defined below, and $r\left(\mathbf{x},\boldsymbol{\lambda},\tau\right)$ are space- and time-lag extended images:

$$\begin{aligned} r\left(\mathbf{x},\boldsymbol{\lambda},\tau\right) &= \sum_j \sum_\omega \overline{u_s\left(j,\mathbf{x}-\boldsymbol{\lambda},\omega\right)} u_r\left(j,\mathbf{x}+\boldsymbol{\lambda},\omega\right) e^{2i\omega\tau} \\ &= \sum_j \sum_\omega T\left(-\boldsymbol{\lambda}\right) \overline{u_s\left(j,\mathbf{x},\omega\right)} T\left(\boldsymbol{\lambda}\right) u_r\left(j,\mathbf{x},\omega\right) e^{2i\omega\tau} \ , \end{aligned} \tag{4}$$

the overline represents complex conjugate. The operator T represents the space shift applied to the wavefields and is defined by

$$T\left(\boldsymbol{\lambda}\right) u\left(j,\mathbf{x},\omega\right) = u\left(j,\mathbf{x}+\boldsymbol{\lambda},\omega\right) \ , \tag{5}$$

The mask operator $K_I\left(\mathbf{x}\right)$ restricts the construction of extended images to chosen discrete locations only, such that the CIPs are constructed only on reflectors and are sampled sparsely in the subsurface. For two reasons, CIPs provide an effective and efficient way to extract velocity information from migrated images. First, no gathers are computed in areas without reflections so the computational cost can be reduced. Second, CIPs can be computed on steep reflectors where conventional CIGs fail to access the velocity information contained in these reflections. An example of a penalty operator $P\left(\boldsymbol{\lambda},\tau\right)$ for vector lags is

$$P\left(\boldsymbol{\lambda},\tau\right) = \sqrt{|\boldsymbol{\lambda}\cdot\mathbf{q}|^2 + \left(V\tau\right)^2} \ . \tag{6}$$

Here $\mathbf{q}$ is a unit vector in the reflection plane and $V\left(\mathbf{x}\right)$ represents the local migration velocity. The operator $P\left(\boldsymbol{\lambda},\tau\right)$ penalizes energy away from zero space- and time-lags, which indicates the existence of velocity errors. Hence, the defocused energy outside zero space-lag is enhanced by the operator $P\left(\boldsymbol{\lambda},\tau\right)$ and forms a residual that is the basis for optimization. Figures 1(a) and 1(b) show penalty operators for CIPs on horizontal and vertical reflectors, respectively. The penalty operator defined in equation 6 represents a cylinder oriented normal to the reflector in the $\boldsymbol{\lambda} - \tau$ space. If we consider only the case of horizontal space-lags, the penalty operator can be simplified as

$$P\left(\boldsymbol{\lambda},\tau\right) = \sqrt{|\boldsymbol{\lambda}|^2 + \left(V\tau\right)^2} \ , \tag{7}$$

where the space-lag vector $\boldsymbol{\lambda} = \{\lambda_x, \lambda_y, 0\}$.

Given $\mathcal{H}_{\boldsymbol{\lambda},\tau}$ in equation 3, the adjoint sources are computed as OF's derivatives with respect to the state variables u_s and u_r (Shen and Symes, 2008). In this case, the adjoint sources g_s and g_r are complicated because the complete lags

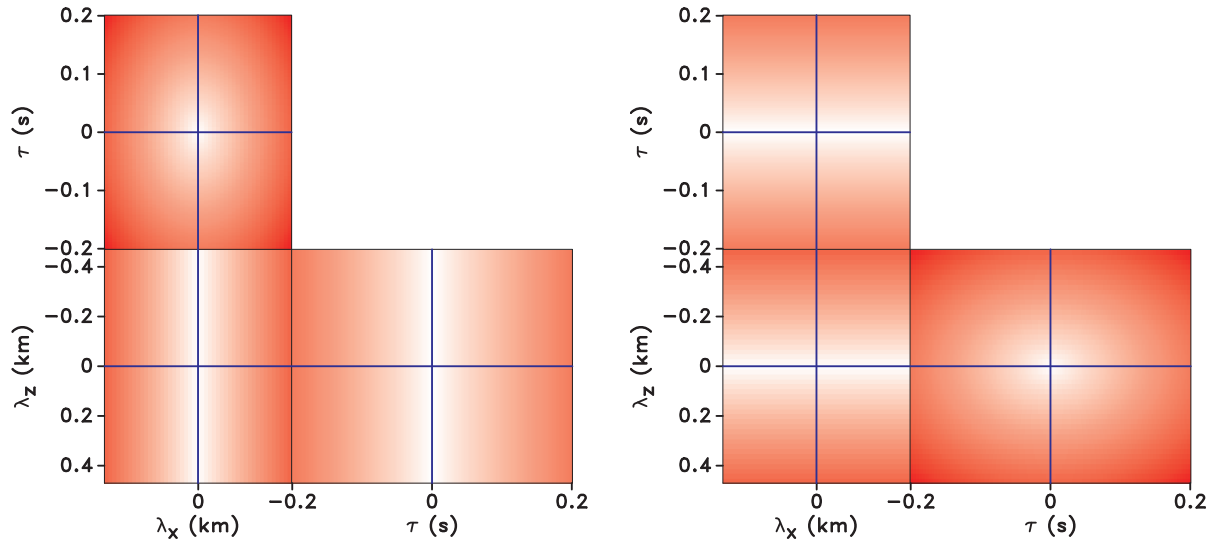


Figure 1. The penalty operators for CIPs on (a) horizontal reflector and (b) vertical reflector.

are involved in the computation.

$$
\begin{aligned}
g_s\left(j,\mathbf{x},\omega\right) &= \sum_{\boldsymbol{\lambda},\tau} T\left(\boldsymbol{\lambda}\right) P\left(\boldsymbol{\lambda},\tau\right) K_I\left(\mathbf{x}\right) \overline{K_I\left(\mathbf{x}\right) P\left(\boldsymbol{\lambda},\tau\right)} \\
&\quad \overline{r\left(\mathbf{x},\boldsymbol{\lambda},\tau\right)} T\left(\boldsymbol{\lambda}\right) u_r\left(j,\mathbf{x},\omega\right) e^{-2i\omega\tau} \\
g_r\left(j,\mathbf{x},\omega\right) &= \sum_{\boldsymbol{\lambda},\tau} T\left(-\boldsymbol{\lambda}\right) P\left(\boldsymbol{\lambda},\tau\right) K_I\left(\mathbf{x}\right) \overline{K_I\left(\mathbf{x}\right) P\left(\boldsymbol{\lambda},\tau\right)} \\
&\quad r\left(\mathbf{x},\boldsymbol{\lambda},\tau\right) T\left(-\boldsymbol{\lambda}\right) u_s\left(j,\mathbf{x},\omega\right) e^{-2i\omega\tau}
\end{aligned}
\tag{8}
$$

The adjoint state variables a_s and a_r are the wavefields obtained by backward and forward modeling respectively, using the corresponding adjoint sources defined in equation 8:

$$
\begin{bmatrix} \mathcal{L}^*\left(\mathbf{x},\omega,m\right) & 0 \\ 0 & \mathcal{L}\left(\mathbf{x},\omega,m\right) \end{bmatrix} \begin{bmatrix} a_s\left(j,\mathbf{x},\omega\right) \\ a_r\left(j,\mathbf{x},\omega\right) \end{bmatrix} = \begin{bmatrix} g_s\left(j,\mathbf{x},\omega\right) \\ g_r\left(j,\mathbf{x},\omega\right) \end{bmatrix} , \tag{9}
$$

and $\mathcal{L}$ and $\mathcal{L}^*$ are the same wave propagation operators used in equation 1.

The last step of the gradient computation is simply the correlation between state variables and adjoint state variables (Plessix, 2006):

$$
\frac{\partial \mathcal{H}_{\boldsymbol{\lambda},\tau}}{\partial m} = \sum_j \sum_\omega \frac{\partial \mathcal{L}}{\partial m} \left(u_s\left(j,\mathbf{x},\omega\right) \overline{a_s\left(j,\mathbf{x},\omega\right)} + u_r\left(j,\mathbf{x},\omega\right) \overline{a_r\left(j,\mathbf{x},\omega\right)} \right) , \tag{10}
$$

where $\frac{\partial \mathcal{L}}{\partial m}$ is the partial derivative of the wave propagation operator with respect to the model parameter. Using the definition of $\mathcal{L}$ in equation 2, we find that $\frac{\partial \mathcal{L}}{\partial m}$ is simply $-\omega^2$. In equation 10 Note that the gradient for image-domain wavefield tomography consists of two correlations because we define both the source and receiver wavefields as the state variables. In contrast, the gradient computed in the data-domain approach involves only one correlation on the source side because we use only the simulated wavefield as the state variable.

An alternative to image-domain wavefield tomography is using space-lag CIGs, just as for conventional DSO (Shen and Symes, 2008). We reformulate the derivation to highlight the similarity between these two approaches. The state variables are also the source and receiver wavefields u_s and u_r simulated by equation 1. The OF based on space-lag CIGs (as opposed to space- and time-lag CIPs) is

$$
\mathcal{H}_{\boldsymbol{\lambda}} = \frac{1}{2} \| K_I\left(\mathbf{x}\right) P\left(\boldsymbol{\lambda}\right) r\left(\mathbf{x},\boldsymbol{\lambda}\right) \|^2_{\mathbf{x},\boldsymbol{\lambda}} , \tag{11}
$$

where

$$
\begin{aligned}
r\left(\mathbf{x},\boldsymbol{\lambda}\right) &= \sum_j \sum_\omega \overline{u_s\left(j,\mathbf{x}-\boldsymbol{\lambda},\omega\right)} u_r\left(j,\mathbf{x}+\boldsymbol{\lambda},\omega\right) \\
&= \sum_j \sum_\omega T\left(-\boldsymbol{\lambda}\right) \overline{u_s\left(j,\mathbf{x},\omega\right)} T\left(\boldsymbol{\lambda}\right) u_r\left(j,\mathbf{x},\omega\right) .
\end{aligned}
\tag{12}
$$

The penalty operator $P\left(\boldsymbol{\lambda}\right)$ annihilates the focused energy at zero lag and highlights the energy of residual moveout at nonzero lag (Shen and Symes, 2008):

$$
P\left(\boldsymbol{\lambda}\right) = |\boldsymbol{\lambda}| . \tag{13}
$$

In practice, it is common to restrict the space-lags in the horizontal directions only, i.e., $\boldsymbol{\lambda} = \{\lambda_x, \lambda_y, 0\}$. The OF $\mathcal{H}_{\boldsymbol{\lambda}}$ is minimized when the reflections focus at zero lag, an indication of the correct velocity model. This, however, occurs only when the subsurface is well illuminated. Otherwise, imbalanced illumination can result in defocusing in the gathers even if the velocity model is correct (Yang et al., 2012). To mitigate the negative influence of the uneven subsurface illumination, we can employ a weighting function that gives low weight on the

gathers in poor illumination areas and puts more weight on the gathers in good illumination areas. As a result, the gathers that are defocused where illumination is poor contribute less to the velocity updates.

Similar to the previous case, the adjoint sources are computed as the derivatives of the OF $\mathcal{H}_{\boldsymbol{\lambda}}$ in equation 11 with respect to the state variables u_s and u_r:

$$\begin{aligned} g_s\left(j,\mathbf{x},\omega\right) &= \sum_{\boldsymbol{\lambda}} T\left(\boldsymbol{\lambda}\right) P\left(\boldsymbol{\lambda}\right)\ K_I\left(\mathbf{x}\right) \overline{K_I\left(\mathbf{x}\right)} \\ &\quad \overline{r\left(\mathbf{x},\boldsymbol{\lambda}\right)} T\left(\boldsymbol{\lambda}\right) u_r\left(j,\mathbf{x},\omega\right) \\ g_r\left(j,\mathbf{x},\omega\right) &= \sum_{\boldsymbol{\lambda}} T\left(-\boldsymbol{\lambda}\right) P\left(\boldsymbol{\lambda}\right)\ K_I\left(\mathbf{x}\right) \overline{K_I\left(\mathbf{x}\right)} \\ &\quad r\left(\mathbf{x},\boldsymbol{\lambda}\right) T\left(-\boldsymbol{\lambda}\right) u_s\left(j,\mathbf{x},\omega\right)\ . \end{aligned} \tag{14}$$

The adjoint state variables a_s and a_r are computed using equation 9 given the adjoint sources defined in equation 8, and the gradient corresponding to the OF in equation 11 is computed as in equation 10.

The derivation above shows the construction of OF and detailed gradient computation for image-domain wavefield tomography. Given these two components, the solution to the inverse problem is found by minimizing the OF using nonlinear gradient-based iterative methods. In each iteration, the gradient is computed and the model update is calculated by line search in the steepest descent or conjugate gradient directions. (Vigh and Starr, 2008b) This procedure is similar to that in data-domain waveform inversion.

3 EXAMPLES

In this section, we illustrate our method with two synthetic examples and emphasize the advantages of using CIPs for velocity model building. The first example highlights the robustness of CIPs in the presence of steeply dipping reflectors. The second example demonstrates the ability of CIPs to reconstruct velocity models in complex subsurface regions.

The first synthetic model is shown in Figure 2(a), and the initial model is just the vertical gradient extended to the entire model. Figures 2(b)-2(c) show the images migrated using RTM with correct and initial velocities, respectively. The lack of 2D circular low-velocity anomaly in the initial model causes defocusing and image triplications.

To highlight the robustness of CIPs, we construct both the CIGs and CIPs in the subsurface at the positions indicated by the vertical lines and dots in Figure 2(c). Figures 3(a)-3(d) and Figures 4(a)-4(d) plot the CIGs and CIPs constructed on different reflectors for correct and initial velocities. Figures 3(c)-3(d) and 4(c)-4(d) compare the CIGs and CIPs constructed on the horizontal reflector. Here, both CIGs and CIPs correctly characterize the reflection as the gathers show either focused reflections or residual moveout depending on the model used for imaging. Thus, one can assess the accuracy of the velocity models by analyzing the focusing information in the gathers. In contrast, Figures 3(a)-3(b) and 4(a)-4(b) show that for the vertical reflector, only CIPs are able to correctly characterize the reflection and thus provide velocity information for the model building. The CIGs are contaminated by artifacts because we construct the gathers using horizontal lags for vertical reflections. The reflections are sampled at every depth level in the gathers, and thus their focusing cannot be correctly characterized. The difference between CIPs and CIGs is caused by the fact that both vertical and horizontal space-lags are used in CIPs while only the horizontal space-lag is used to construct CIGs. Therefore, CIGs are biased towards reflectors with small dips and fail to evaluate the velocity information available in steep reflectors. For CIPs, one can evaluate the model accuracy by analyzing focusing of vertical and horizontal reflectors in the $\lambda_z - \tau$ and $\lambda_x - \tau$ panels, respectively: the vector space-lags and time-lag of CIPs remove the directional bias toward horizontal reflectors, and CIPs are robust and able to analyze the velocity information from reflections regardless of the subsurface structure.

Next, we use the adjoint-state method as described in the previous section to calculate the gradient for three different scenarios: using CIPs on the horizontal reflector only, using CIPs on the vetical reflector only, and using CIPs on both reflectors. Figure 5(a) plots the difference between the correct and initial velocities. Figures 5(b)-5(d) show the gradient of the objective function computed using different groups of CIPs, indicated by the black dots. Observe that the gradients highlight the target in different ways. The gradient in Figure 5(b) constrains the model variation in the horizontal direction. In contrast, the gradient in Figure 5(c) constrains the model variation in the vertical direction. When the gradient is computed from CIPs picked on both vertical and horizontal reflectors, as shown in Figure 5(d), the variation is more effectively controlled in both the vertical and horizontal directions. Using the gradient computed from all CIPs, we reconstruct the velocity model shown in Figure **??**. The image migrated with this updated model is shown in Figure 6(b). The coherency of both the vertical and horizontal reflectors is improved because of the more accurate gradient used in the inversion. This indicates that using CIPs, especially those sampled on the steeply dipping reflections, we can extract additional information from the migrated image and offer more constrains for the model building.

To show the performance of CIPs in wavefield tomography, we consider the synthetic Marmousi model. The correct velocity model is shown in Figure 7(a). The source locations are evenly distributed on the surface from 1.0 km to 7.0 km at a spacing of 0.1 km. The receiver arrays are fixed for all the shots and span entirely the surface at a spacing of 0.01 km. The data are generated via finite-difference Born modeling, using a Ricker wavelet with peak frequency of 15 Hz. The data are then transformed into the frequency domain because both the migration and wavefield tomography operators are based on the frequency-domain downward continuation method. In this way, we avoid using the same operator for both the modeling and inversion procedures. The image, space-lag gathers, and angle gathers migrated with the true velocity model are shown in Figures 7(b)-7(d). As one might expect, reflections in the space-lag gathers are focused at zero offset, and events in the angle gathers are flat because the correct model is used for mi-

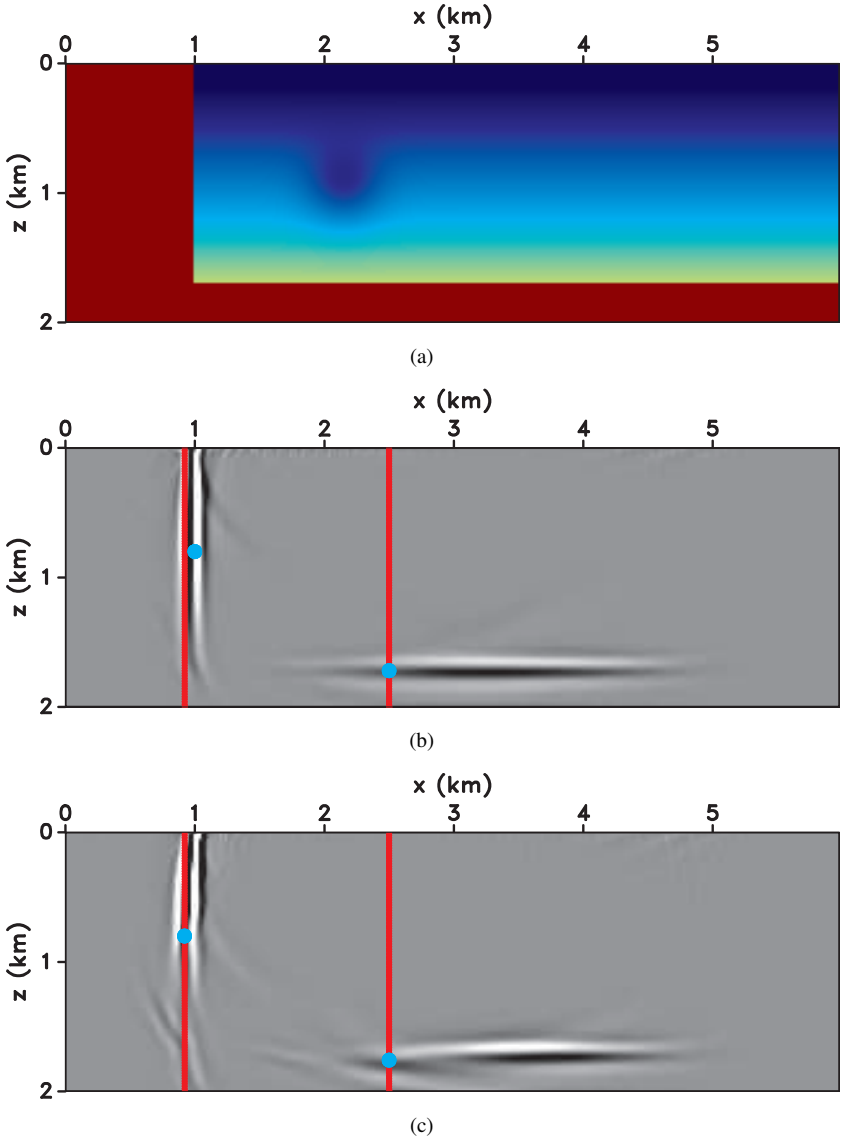


Figure 2. (a) The true velocity model. The images migrated with (b) the true velocity model, and (c) the initial velocity model.

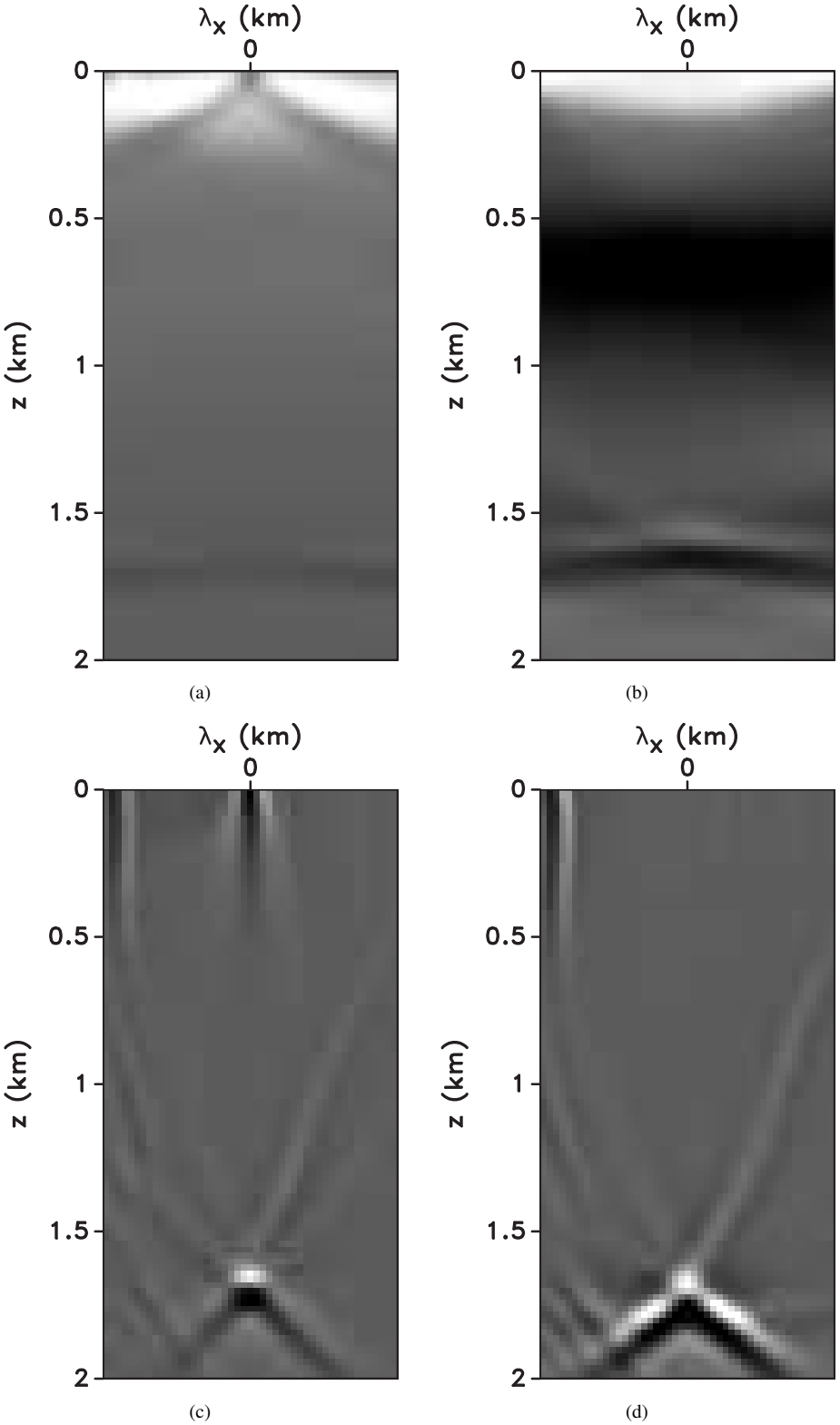


Figure 3. The space-lag CIGs constructed for the vertical reflector at x=1 km migrated with (a) the correct velocity, (b) the initial velocity, and CIGs at constructed for the horizontal reflector x=2.5 km migrated with (c) the correct velocity, (d) the initial velocity.

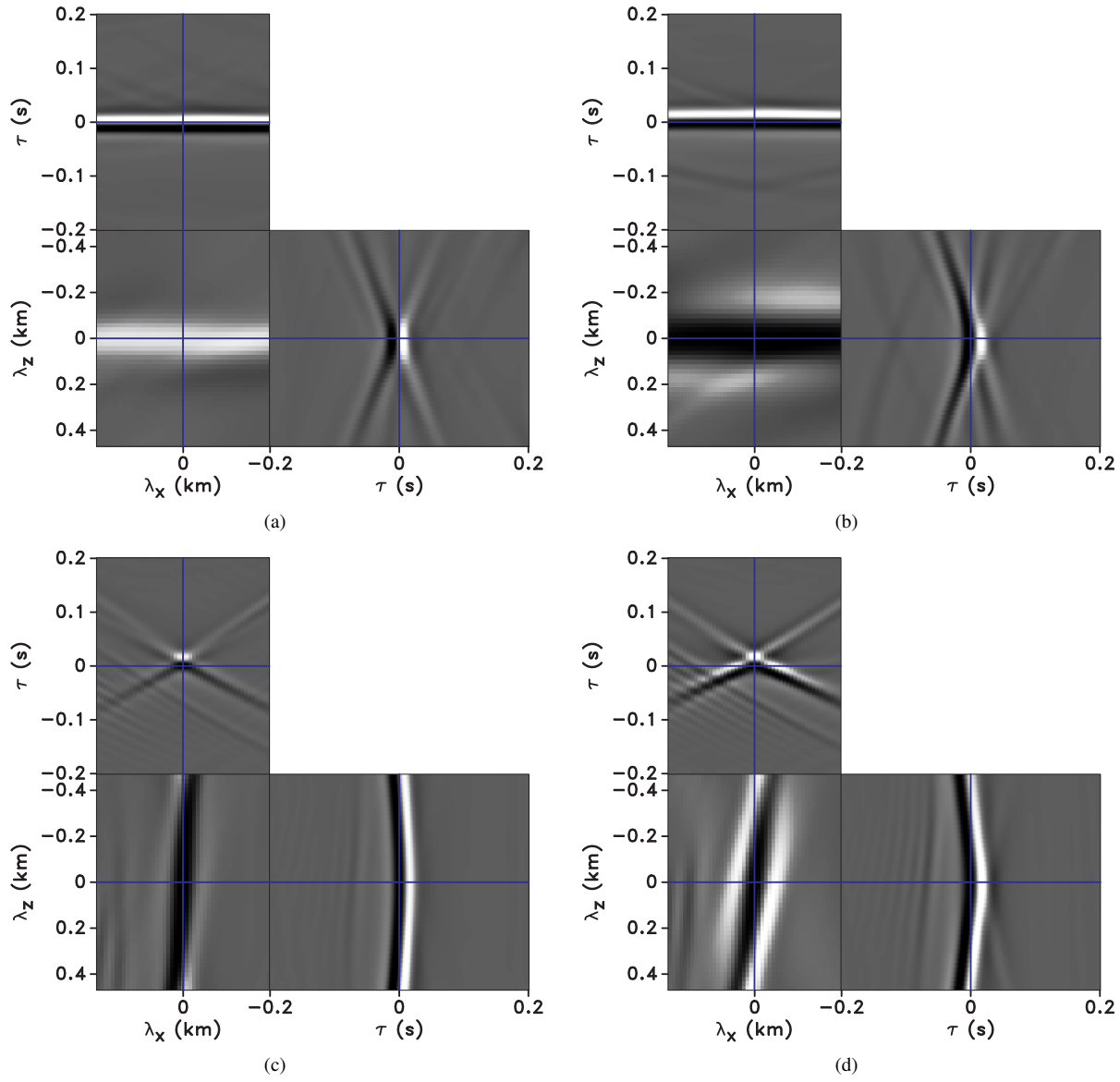


Figure 4. The CIPs at x=1 km, z=0.8 km migrated with (a) the correct velocity, (b) the initial velocity, compared with Figures 3(a) and 3(b). CIPs at x=1.7 km, z=2.5 km migrated with (c) the correct velocity, (d) the initial velocity , compared with Figures 3(c) and 3(d).

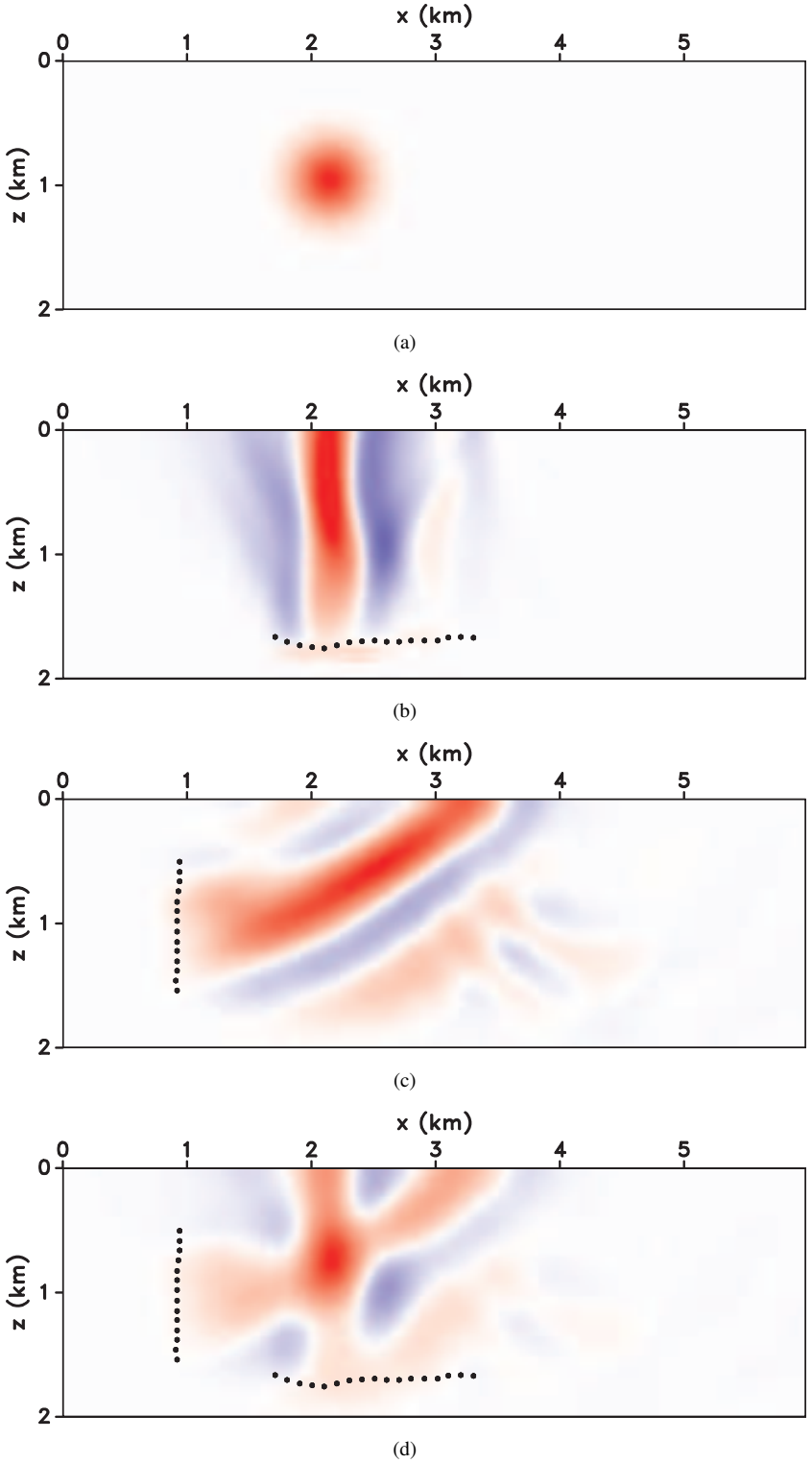


Figure 5. (a) The true velocity variation which is the target of inversion. The gradient constructed from (b) CIPs on the horizontal reflector only, (c) CIPs on the vertical reflector only, (d) CIPs on both the horizontal and vertical reflectors.

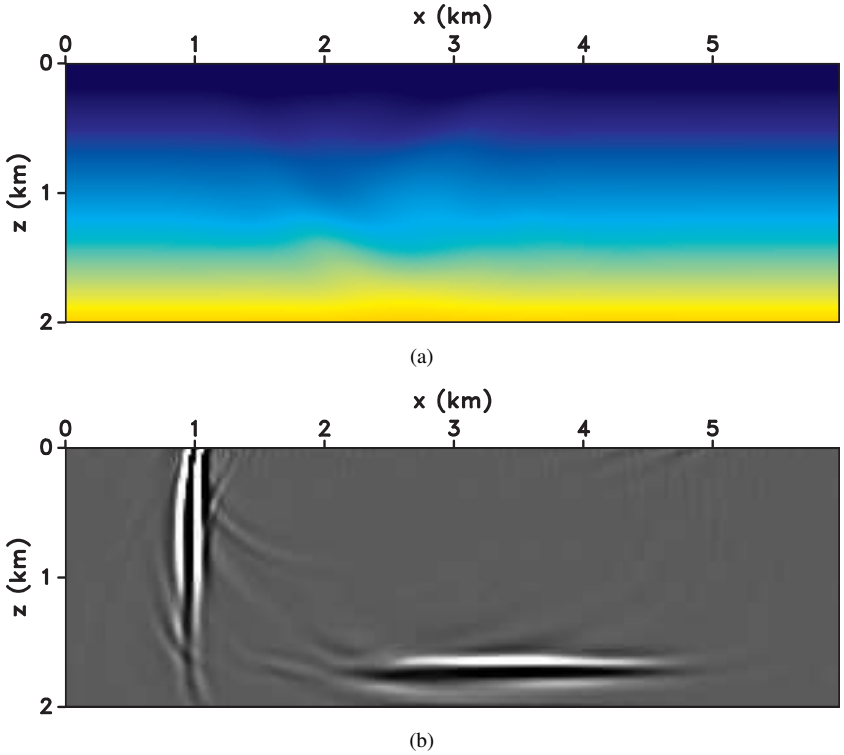


Figure 6. (a) The reconstructed velocity model. (b) The migrated image using the updated model.

gration. The initial model used for the inversion, Figure 8(a), is a highly smoothed version of the true model. This model resembles the results one can obtain from conventional ray-based reflection tomography. Figures 8(b)-8(d) show the image, space-lag gathers, and angle-domain CIGs migrated with the initial model. Since the initial model is highly smoothed, it lacks the necessary components required by the migration to produce an accurate result. Thus, the migrated image exhibits severe distortions in the reservoir region around $x = 5$ km, $z = 2.5$ km. The reduced image quality can be further confirmed by the defocused energy in the space-lag gather and the residual moveout in the angle gathers, as shown in Figures 8(c) and 8(d). In our example, the angle gathers are used only for quality control, rather than for velocity model building.

We initiate our velocity analysis process by selecting common-image-point gather locations at which we construct extended images necessary for velocity analysis. These locations are selected using the automatic picking algorithm developed by Cullison and Sava (2011). Figure 8(b) shows the picked locations overlain on the image. They follow the coherent structure of the image, and tend to be randomly positioned where the reflections are less coherent. Figure 9 shows the weighting function we apply to the input gathers in order to compensate for the uneven illumination in the subsurface. Light colors indicate low values of the weights applied in the poor illumination areas, and dark colors indicate high value of the weights applied in the good illumination areas. This weighting function is included in the objective function to speed up the convergence of the inversion. Figures 10(a) and 10(b) show the inverted model after 20 nonlinear iterations and the corresponding migrated image. From the result, it is apparent that the updated velocity model significantly improves the imaging quality as the reservoir area is better focused and more coherent in the migrated image. In addition, the reflections are focused in space-lag gathers and flatter in angle gathers, as shown in Figures 10(c) and 10(d), as compared with those in Figures 8(c) and 8(d). These also indicate the improvement on the image due to the velocity update.

4 DISCUSSION

The synthetic examples demonstrate the successful velocity model updates produced by our approach using CIPs. In the first example, we show that CIPs do not bias their sensitivity toward any particular direction compared to the more conventional CIGs which sample image points more densely in the vertical direction than lateral direction. From the gradient computation, we notice that the CIPs located along nearly horizontal reflectors provide higher resolution laterally, whereas the CIPs located along nearly vertical reflectors provide higher resolution vertically.

In the second synthetic example, only the horizontal space lag and time lag are involved in CIPs computation. The vertical space lag is not required because there are no steeply dipping reflectors in the model. We thus significantly reduce

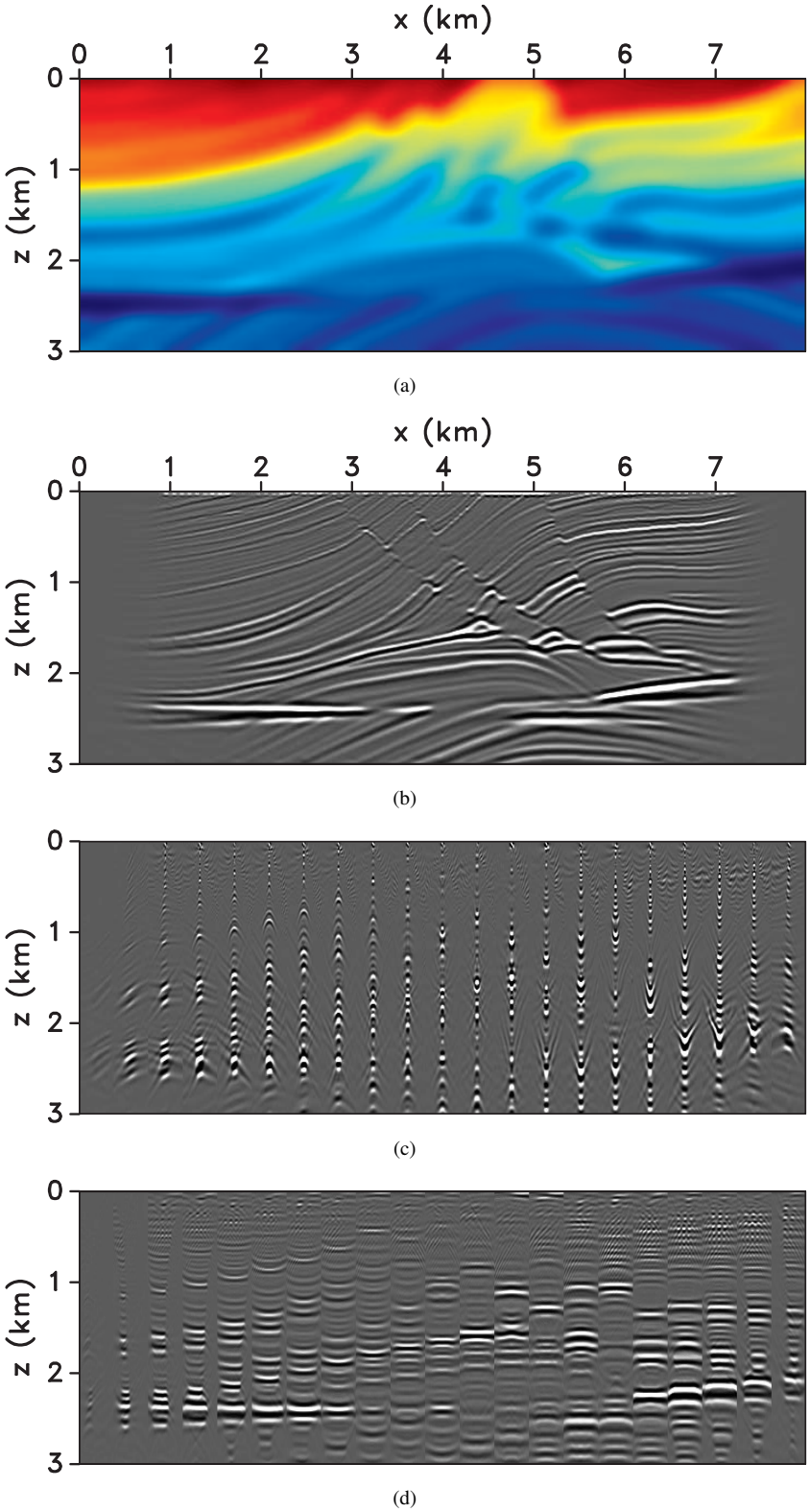


Figure 7. (a) The true model used to generate the data. (b) The migrated image, (c) the space-lag gathers, and (d) the angle-domain gathers obtained using the true model.

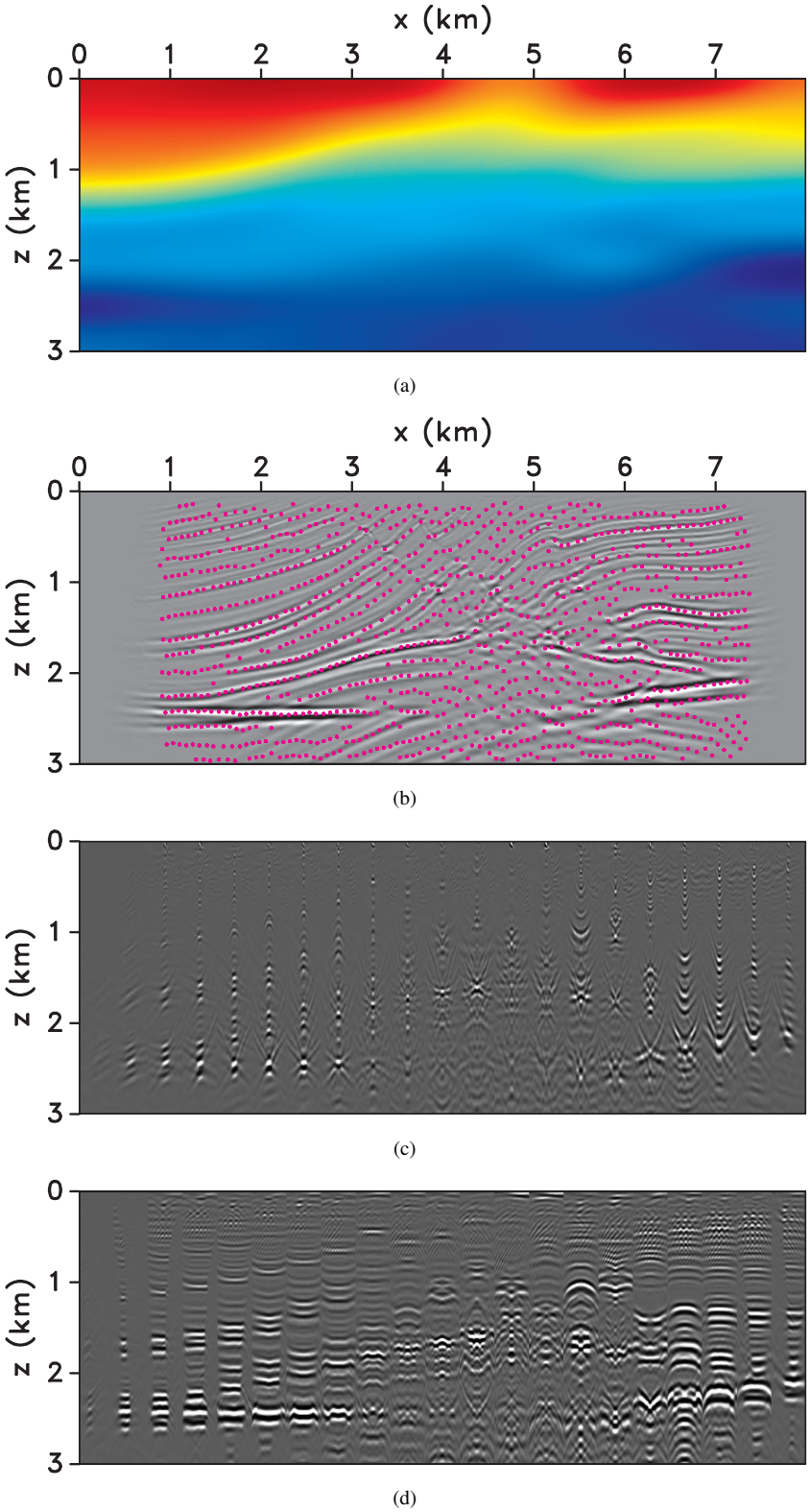


Figure 8. (a) The initial model used in the velocity inversion. (b) The migrated image overlain with the CIPs location, (c) the space-lag gathers, and (d) the angle-domain gathers obtained using the initial model.

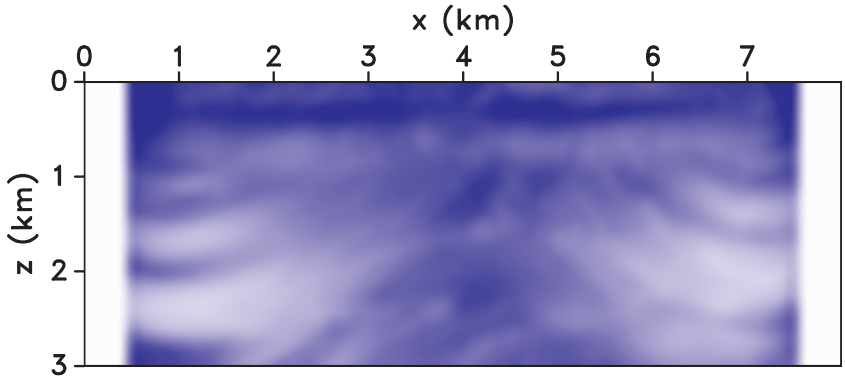


Figure 9. The weighting function based on the subsurface illumination.

the cost for computing and storing the gathers for velocity analysis. After running the inversion, the main features of the model are resolved and they help improving the quality of the image. The improvements can be directly observed from the more coherent image, more focused reflections in space-lag gathers, and flatter events in angle gathers. The results demonstrate our image-domain wavefield tomography based on CIPs can achieve similar results to conventional methods but with reduced computational effort. This is especially crucial for velocity analysis in large-scale 3D applications.

5 CONCLUSIONS

We demonstrate a wavefield-based velocity model building method implemented in the image domain. The procedure optimizes the velocity model by minimizing the image incoherency caused by model errors. The objective function is particularly designed for common-image-point gathers constructed locally on the reflection event. The penalty operator used in the objective function is aimed at improving the focusing of the reflections in the gathers.

The two synthetic examples demonstrate the main advantages of using CIPs over conventional subsurface-offset common-image gathers in the wave-equation tomographic approach. First, the CIPs avoid the bias toward horizontal reflection events and thus are more robust in analyzing velocity information for steeply dipping structure in the complex geologic regions. Second, CIPs significantly reduce the cost for computing and storing the extended images compared with more conventional common-image gathers while producing reliable model updates. This is mainly attributed to the optimized sampling of CIPs in the subsurface as only the significant reflections are analyzed to provide information for velocity update.

6 ACKNOWLEDGMENTS

We acknowledge the support of the sponsors of the Center for Wave Phenomena at Colorado School of Mines. The reproducible numeric examples in this paper use the Madagascar open-source software package freely available from http://www.reproducibility.org. This research was supported in part by the Golden Energy Computing Organization at the Colorado School of Mines using resources acquired with financial assistance from the National Science Foundation and the National Renewable Energy Laboratory.

REFERENCES

Al-Yahya, K., 1989, Velocity analysis by iterative profile migration: Geophysics, **54**, 718–729.

Biondi, B., and W. Symes, 2004, Angle-domain common-image gathers for migration velocity analysis by wavefield-continuation imaging: Geophysics, **69**, 1283–1298.

Cullison, T., and P. Sava, 2011, An image-guided method for automatically picking common-image-point gathers: Presented at the 81th Annual International Meeting, SEG, Expanded Abstracts.

Etgen, J., S. H. Gray, and Y. Zhang, 2009, An overview of depth imaging in exploration geophysics: Geophysics, **74**, WCA5–WCA17.

Gao, F., and W. Symes, 2009, Differential semblance velocity analysis by reverse time migration: Image gathers and theory: 77th Annual International Meeting, SEG, Expanded Abstracts, 2317–2320.

Gray, S. H., J. Etgen, J. Dellinger, and D. Whitmore, 2001, Seismic migration problems and solutions: Geophysics, **66**, 1622–1640.

Mulder, W. A., 2008, Automatic velocity analysis with the two-way wave equation: Presented at the 70th EAGE Conference and Exhibition, Extended Abstracts.

Plessix, R.-E., 2006, A review of the adjoint state method for computing the gradient of a functional with geophysical applications: Geophysical Journal International, **167**, 495–503.

———, 2009, Three-dimensional frequency-domain full-waveform inversion with an iterative solver: Geophysics, **74**, WCC53–WCC61.

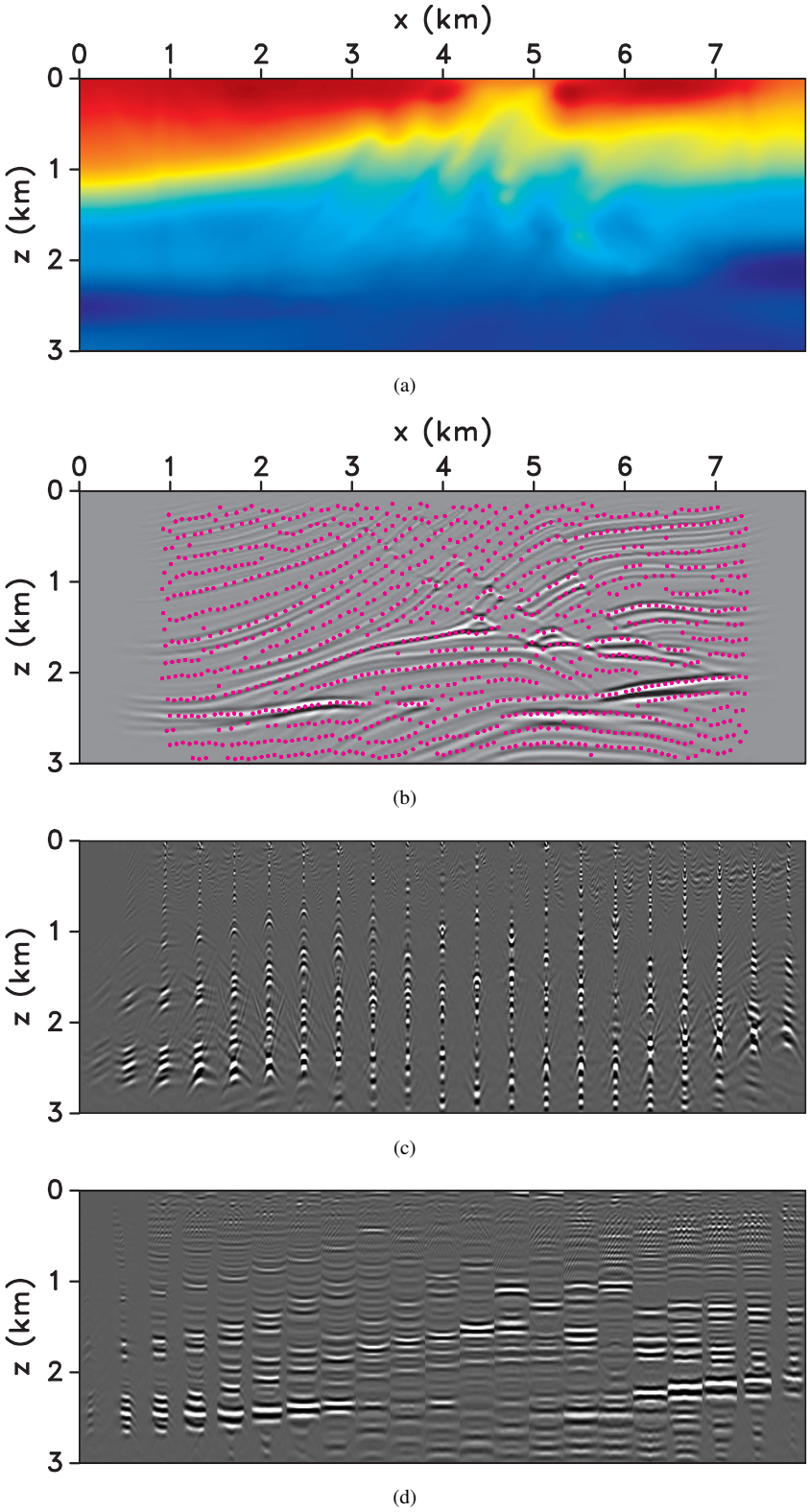


Figure 10. (a) The updated model after 20 iterations of inversion using CIPs. (b) The migrated image overlain with the CIPs locations, (c) the space-lag gathers, and (d) the angle-domain gathers obtained using the updated model.

Pratt, R. G., 1999, Seismic waveform inversion in the frequency domain, Part 1: Theory and verification in a physical scale model: Geophysics, **64**, 888–901.

Rickett, J., and P. Sava, 2002, Offset and angle-domain common image-point gathers for shot-profile migration: Geophysics, **67**, 883–889.

Sava, P., and B. Biondi, 2004a, Wave-equation migration velocity analysis - I: Theory: Geophysical Prospecting, **52**, 593–606.

———, 2004b, Wave-equation migration velocity analysis - II: Subsalt imaging examples: Geophysical Prospecting, **52**, 607–623.

Sava, P., B. Biondi, and J. Etgen, 2005, Wave-equation migration velocity analysis by focusing diffractions and reflections: Geophysics, **70**, U19–U27.

Sava, P., and S. Fomel, 2003, Angle-domain common image gathers by wavefield continuation methods: Geophysics, **68**, 1065–1074.

———, 2006, Time-shift imaging condition in seismic migration: Geophysics, **71**, S209–S217.

Sava, P., and I. Vasconcelos, 2011, Extended imaging condition for wave-equation migration: Geophysical Prospecting, **59**, 35–55.

Sava, P., and I. Vlad, 2008, Numeric implementation of wave-equation migration velocity analysis operators: Geophysics, **73**, VE145–VE159.

Shen, P., and H. Calandra, 2005, One-way waveform inversion within the framework of adjoint state differential migration: 75th Annual International Meeting, SEG, Expanded Abstracts, 1709–1712.

Shen, P., and W. W. Symes, 2008, Automatic velocity analysis via shot profile migration: Geophysics, **73**, VE49–VE59.

Sirgue, L., and R. Pratt, 2004, Efficient waveform inversion and imaging: A strategy for selecting temporal frequencies: Geophysics, **69**, 231–248.

Stolk, C. C., and W. W. Symes, 2004, Kinematic artifacts in prestack depth migration: Geophysics, **69**, 562–575.

Symes, W., 2009, Migration velocity analysis and waveform inversion: Geophysical Prospecting, **56**, 765–790.

Symes, W. W., 2008, Migration velocity analysis and waveform inversion: Geophysical Prospecting, **56**, 765–790.

Symes, W. W., and J. J. Carazzone, 1991, Velocity inversion by differential semblance optimization: Geophysics, **56**, 654–663.

Tarantola, A., 1984, Inversion of seismic reflection data in the acoustic approximation: Geophysics, **49**, 1259–1266.

Vasconcelos, I., P. Sava, and H. Douma, 2010, Nonlinear extended images via image-domain interferometry: Geophysics, **75**, SA105–SA115.

Vigh, D., and E. W. Starr, 2008a, 3D prestack plane-wave, full-waveform inversion: Geophysics, **73**, VE135–VE144.

———, 2008b, Comparisons for waveform inversion, time domain or frequency domain?: 78th Annual International Meeting, SEG, Expanded Abstracts, 1890–1894.

Virieux, J., and S. Operto, 2009, An overview of full-waveform inversion in exploration geophysics: Geophysics, **74**, WCC1–WCC26.

Woodward, M., D. Nichols, O. Zdraveva, P. Whitfield, and T. Johns, 2008, A decade of tomography: Geophysics, **73**, VE5–VE11.

Woodward, M. J., 1992, Wave-equation tomography: Geophysics, **57**, 15–26.

Yang, T., and P. Sava, 2011, Waveform inversion in the image domain: Presented at the 73th EAGE Conference and Exhibition, Extended Abstracts.

Yang, T., J. Shragge, and P. Sava, 2012, Illumination compensation for image-domain wavefield tomography: Presented at the 74th Mtg., Abstracts, Eur. Assoc. Expl. Geophys.

Yilmaz, O., 2001, Seismic Data Analysis (2nd edition): Society of Exploration Geophysicists.